Using unit cell simulations to investigate fracture due to compression-tension loading

Martin Kristoffersen[a,*], Tore Børvik[a], Odd Sture Hopperstad[a]

[a]*Structural Impact Laboratory (SIMLab),*
Department of Structural Engineering, Norwegian University of Science and Technology (NTNU),
Rich. Birkelands vei 1A, NO-7491 Trondheim, Norway

Abstract

Experiments regarding impact against X65 steel pipes show that fracture typically arises in areas subjected to large compressive strains before tension. Fracture surfaces from these areas are brittle in character despite the material exhibiting ductile behaviour elsewhere. Smooth and notched tensile material tests always produced ductile fracture through nucleation, growth and coalescence of voids. The ductile-to-brittle transition seen in the component tests was however recreated in notched axisymmetric material tests, where the specimens were compressed to various levels of plastic strain before being stretched to failure. Increasing compression before tension showed a decrease in strain to fracture as hypothesised, and an increase in the cleavage surface fraction. In an attempt to gain a better understanding of this behaviour, unit cell simulations subjected to tension only and compression-tension loading were carried out. As well as exploring different chosen stress triaxialities, global analyses of the material tests were used to provide an average stress triaxiality for the axisymmetric unit cell simulations. These global simulations were able to represent the material tests with good accuracy. In tension tests where the stress triaxiality was fairly constant (notched tests), the unit cell analyses were able to predict a strain to coalescence within reasonable margin compared with the experimental values. Unit cell simulations including the compressive phase show that the higher the magnitude of the stress triaxiality is during compression, the higher the local stress in the cell, which in turn may trigger cleavage fracture.

Keywords: Material tests, unit cell simulations, compression-tension load, ductile fracture, cleavage fracture

1. Introduction

Today and for all foreseeable future, steel pipelines are and will be used extensively for transporting oil and gas. These pipelines are situated in potentially dangerous environments, where impact loads from e.g. anchors or trawl gear pose a particularly hazardous threat [1].

---
*Corresponding author, tel.: +47-73-55-10-48; fax: +47-73-59-47-01

Pipe impact tests have shown that fracture is likely to occur directly underneath the striker during the elastic recovery after maximum displacement [2, 3]. In this area of the pipe the material is heavily compressed before the loading is reversed into tension which can cause a ductile-to-brittle transition [4]. Earlier, Ludley and Drucker [5] made bent-beam specimens which emulates the strain history from the pipe (compression followed by tension), and a ductile-to-brittle transition was observed at room temperature for an estimated 60% precompression.

Several studies have considered material behaviour subsequent to a prescribed prestrain. Drucker et al. [6] compressed cylindrical specimens in the range of 10% to at most 45% strain, where the specimens were machined to their original shape for approximately each 3% strain increment to ensure as uniform compression as possible. When stretching axisymmetric unnotched tensile specimens machined from the cyldinders after this procedure, a reduction of the tensile strain to failure was observed with increasing precompression. Further, a plastic prestrain history has been shown to elevate the crack tip stress field in a single-edge notched tensile specimen made from pipeline steels [7]. Fukuda et al. [8] demonstrated that both compressive and tensile prestrain reduced the critical crack tip opening displacement (CTOD) for various offshore steels, where compressive strains had a larger effect than tensile. Notched, axisymmetric specimens from an SM490B steel were first compressed to 10% and 30% and then stretched to failure by Enami [9], and both cases showed signs of local cleavage cracks. Bouchard et al. [10] investigated the effect of particle distribution on reverse loading of ductile steels, while Bao and Wierzbicki [11] used notched and cylindrical specimens for compression testing of a 2024-T351 aluminium alloy, in which fracture initiated by shear in the equatorial area. For the same alloy, combined tension/compression/torsion experiments on tubular specimens were carried out by Papasidero et al. [12]. Their experimental results indicated that precompression can increase the ductility of aluminum 2024-T351. Notched specimens were used by Kristoffersen et al. [4], and compressed to large values of true strain (up to 1.00) before being stretched to failure in tension. Cleavage fracture was observed in many cases along with particles (sometimes cracked) around which voids seem to nucleate [13]. Cracks in particles can propagate into the matrix, thereby causing cleavage fracture [14].

Computational unit cells have been used for decades, and have proved to be a helpful tool in understanding the fracture process. From the early works of Tvergaard [15] and Koplik and Needleman [16], to more recent studies (see e.g. Tian et al. [17]), important insight has been gained on the ductile fracture process under various (typically positive) stress triaxialities and Lode angles [18–23]. The effect of tensile prestrain on the subsequent strain to void coalescence was studied numerically by Zhang and Skallerud [24], where it was shown that the prestrain generally reduced the strain to coalescence. By loading cells in uniaxial tension to a certain strain level and thereafter applying a specified constant triaxiality, Benzerga et al. [25] showed that a time-weighted average triaxiality does not necessarily produce a unique strain to failure. Including a spherical particle have been shown to reduce the effective strain at the beginning of localisation [26]. Cylindrical carbides may promote cleavage fracture if their aspect ratio is high [27]. More recently, a micromechanical approach using a Gurson-Tvergaard-Needleman (GTN) model combined with a cohesive zone was

employed to model crack propagation with competing ductile and cleavage fracture [28], where going from 2D to 3D was important for accurate results. A critical stress is typically associated with cleavage fracture when it is modelled numerically [29].

Few studies have considered the effect of large compressive strains on subsequent stretching. The importance of the strain path has been discussed [25, 30], and it has been shown that it is important to account for inclusions when applying compressive loads [31]. Experiments by Yoshida et al. [32] showed that dual phase steel features a Bauschinger effect and work-hardening stagnation when subjected to cyclic loading. Compression-tension tests (up to 13% engineering strain) on DP780 dual phase steel sheets using an anti-buckling device indicated that the strain to fracture increased with increasing compression [33].

In this study, axisymmetric unit cells comprised of a "hard" (linear elastic) particle and a "softer" (elasto-plastic) matrix are used to qualitatively explore the effect various levels of compression has on the subsequent tensile behaviour of the cell. Global analyses of the material tests have been used to generate an average stress triaxiality, one for compression and another one for tension, which was applied to the cell. Further, different chosen compressive stress triaxialities have been applied to assess the effect this has on the subsequent tensile behaviour when the tensile triaxiality is equal to unity. In the current work it is shown that an increasing level of compression leads to an increased stress around the stress concentrator (particle) locally in the cell, which prevails through the tensile step and can thereby increase the likelyhood of cleavage fracture [34, 35]. In addition to increasing the general stress level in the cell, increasing the magnitude of the compressive triaxiality (i.e. moving towards $-\infty$ on the real axis) for a given compression level appeared to reduce the strain to coalescence during the subsequent tension, which is in accordance with expectations based on the experiments.

2. Material

2.1. Description

The X65 offshore steel material studied here is commonly used in pipelines transporting oil and gas [36]. Aside from Fe, the main chemical constituents in weight percentage are 0.09 C, 0.25 Si, 1.13 Mn, 0.04 Cr, 0.09 Mo, 0.09 Cu and 0.06 V. Two types of particles were found in the material, spherical and angular as shown in Fig. 1, with the former type consisting of calcium aluminate and the latter type was comprised of titanium and carbon or nitrogen (inconclusive). The spherical particles bonded poorly with the matrix and had a typical size of 1 μm to 10 μm, while the angular particles were less numerous with a size of about 5 μm and bonded well with the matrix. As the spherical particles were the ones found in relation with fracture, these were counted from 13 microscope images measuring approximately 145×110 μm and a particle size distribution was thereby estimated (see Fig. 2) along with an initial particle volume fraction $\omega_0 = 0.0005$, which is what will be used in the unit cell models in Section 5. The microstructure in two different directions is shown in Fig. 3, and a ferritic grain structure with grains of size ≤ 10 μm was observed.

(a) Spherical particle   (b) Angular particle

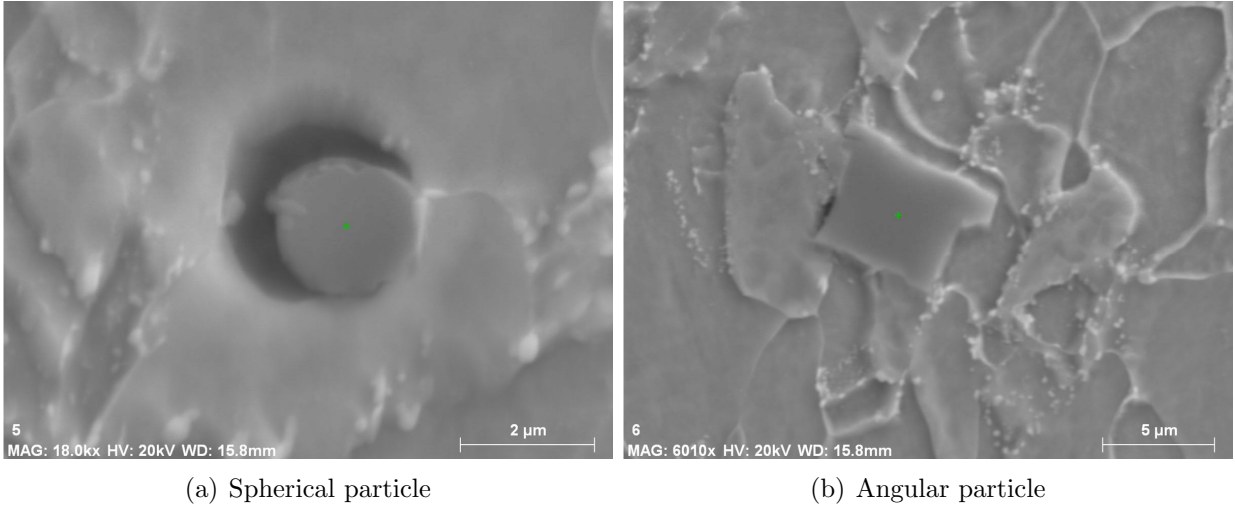Fig. 1: Two types of particles were found in the material, (a) spherical and (b) angular [4].

2.2. Uniaxial tension tests

The material has been characterised as both homogeneous and isotropic [4], and showed moderately increasing flow stress with increasing strain rates [37]. All tests and simulations herein are quasi-static, so this effect will be left unaccounted for. Based on 12 quasi-static uniaxial tensile tests on a smooth geometry (see bottom of Fig. 4(a)), the material has a measured yield stress of 478 ± 15 MPa, an ultimate tensile strength of 572 ± 14 MPa, a true peak stress of $1\,314 \pm 12$ MPa, and a true fracture strain of 1.61 ± 0.03. Fig. 4(b) shows typical true stress-true strain curves until failure for smooth and notched specimens. Young's modulus is $E = 208\,000$ MPa [38]. A summary of three of the smooth tension tests, along with all the notched tension tests, can be seen in Table 1.

All test specimens were taken from the same continuous, seamless pipe. During every
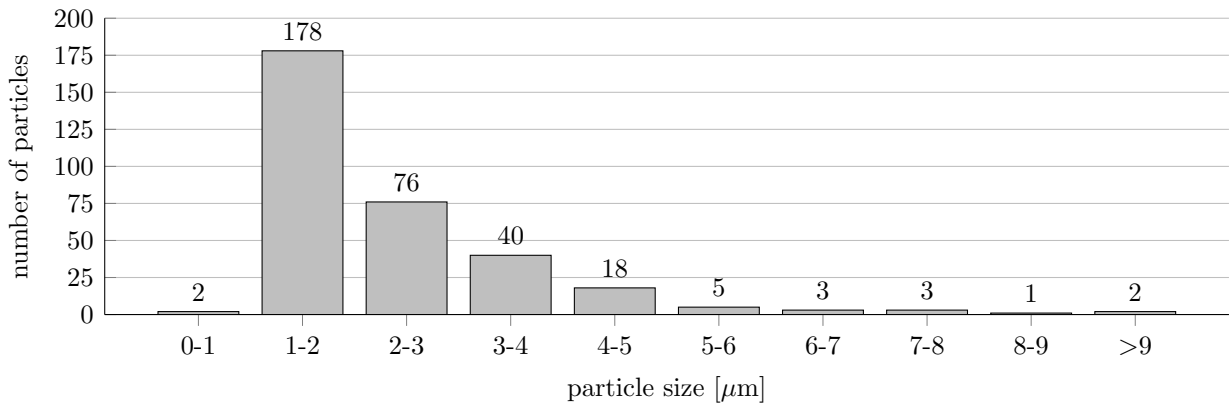

Fig. 2: Particle distribution of spherical particles based on 13 images, with the particle size in μm on the abscissa and the particle count on the ordinate.

4

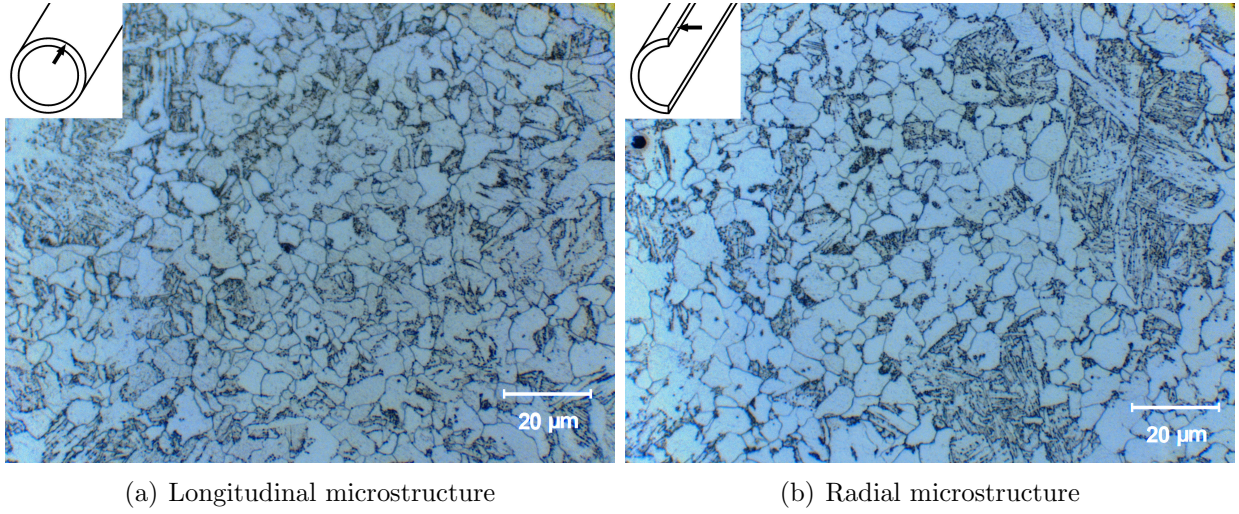(a) Longitudinal microstructure　　　　(b) Radial microstructure

Fig. 3: Microstructure of the material in (a) the longitudinal direction and (b) the radial direction [4].

material test, a laser based measuring device, amply described by Fourmeau et al. [40], was used to continuously keep track of the specimens' smallest diameters D_r and D_θ in two perpendicular directions all the way to fracture. D_r is the diameter in the radial direction with respect to the pipe, and D_θ is in the circumferential direction. The ratio D_r/D_θ was approximately unity throughout the test, indicating an isotropic material. By assuming negligible elastic strains and plastic incompressibility, the true (Cauchy) stress σ and true (logarithmic) strain ε can be calculated from
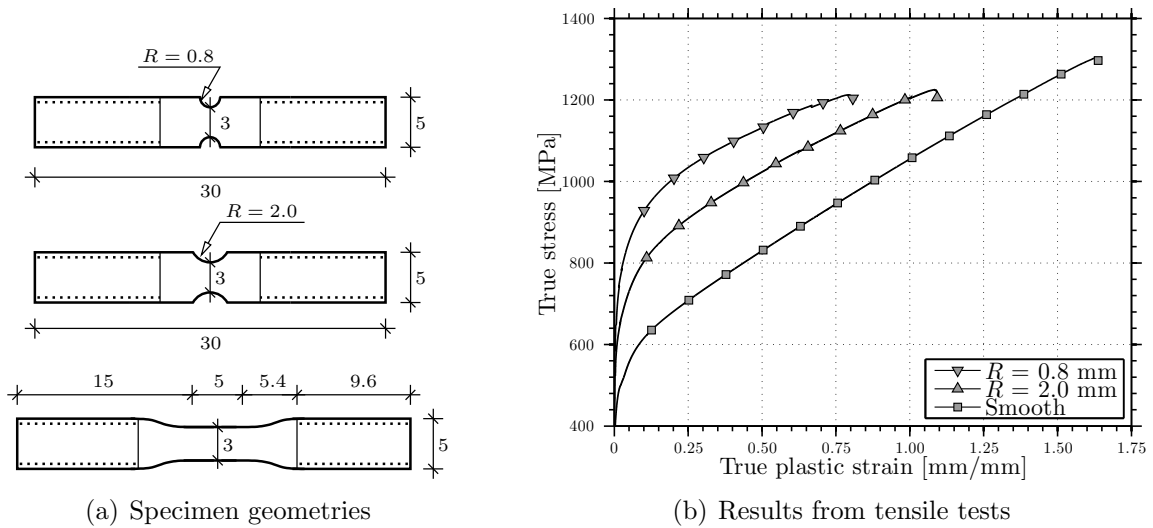

(a) Specimen geometries　　　　(b) Results from tensile tests

Fig. 4: Specimens (a) used in quasi-static tensile tests (measures in mm), and the results thereof (b) [39].

5

$$\sigma = \frac{F}{A}, \qquad\qquad \varepsilon = \ln\left(\frac{A_0}{A}\right) \tag{1}$$

in which F is the force measured by the load cell in the test machine, and A_0 is the specimen's initial cross-sectional area, $A_0 = (\pi/4)\, D_0^2$, with D_0 being the initial diameter. A is the current minimum area of the cross-section, determined by the continuously measured D_r and D_θ, $A = (\pi/4) D_r D_\theta$. The fracture strain ε_f can then be calculated from $\varepsilon_f = \ln(A_0/A_f)$ where A_f is the cross-sectional area of the specimen after fracture. Assuming additive decomposition of the elastic and plastic strains, the plastic strain can be found through $\varepsilon^p = \varepsilon - \sigma/E$. Note that σ and ε in Eq. (1) represent average values over the minimum cross-section.

Continuing with Fig. 4, two types of notched specimens were also tested. Fracture strain clearly decreased when the notch became sharper and the stress triaxiality increased. Stress triaxiality σ^* is defined as the ratio between the hydrostatic stress σ_H and the equivalent von Mises stress σ_{eq}, $\sigma^* = \sigma_H/\sigma_{\mathrm{eq}}$. An estimate for the initial stress triaxiality σ^*_{init} at the center of the specimen is given by Bridgman's analysis [41] assuming plastic incompressibility and a neck shaped like a circular arc,

$$\sigma^*_{\mathrm{init}} = \frac{1}{3} + \ln\left(1 + \frac{a}{2R}\right) \tag{2}$$

where a is the radius of the specimen's minimum cross-sectional area and R is the profile radius of the notch at the root. While the fracture strain decreased with a sharper notch, the stress σ_f at fracture remained within the same order of magnitude (about 7-8% reduction in true stress at fracture when going from a smooth specimen to the sharpest notch). Further, the "work per volume" to failure W_{cr}, as expressed by Cockcroft and Latham [42],

$$W_{\mathrm{cr}} = \int_0^{\varepsilon_f} \langle \sigma_1 \rangle \, \mathrm{d}\varepsilon^p \tag{3}$$

was reduced with increasing triaxiality (see Table 1 for additional details). Here, $\langle \sigma_1 \rangle = \max\{0, \sigma_1\}$ in which σ_1 is the average maximum principal stress, which is equal to the average stress (over the cross-section) measured in Fig. 4(b).

2.3. Compression-tension tests

Two main test geometries D1 and D2 are used for compression-tension loading in this study, both of which are shown in Fig. 5. The diabolo shape is particularly suitable for achieving high levels of compressive strains as barrelling can be kept at a minimum, if not avoided. These specimens were compressed to various levels of true strain before the load was reversed into tension until failure. The D1 samples were compressed to true strain values of 0.10, 0.20, 0.30 and 0.40 before tension, in addition to a case without compression for reference. Next, the D2 samples were compressed to true strain levels of 0.40, 0.60, 0.80 and 0.90 before tension was applied. One D2 specimen was also tested without any compression for reference. The geometry was changed to attain higher levels of compression

6

Table 1: Experimental data from quasi-static tensile tests (see Fig. 4 as well).

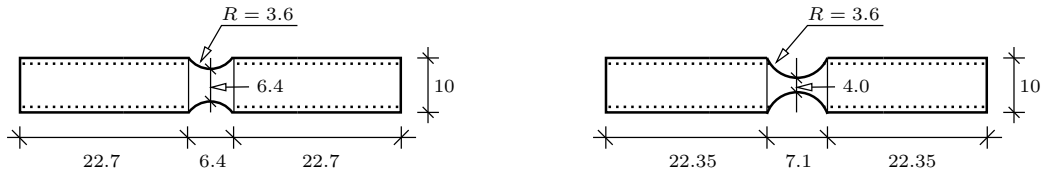| ID	R [mm]	a [mm]	σ^*_{init}	ε_f	σ_f [MPa]	W_{cr} [MPa]
Sm-1	Smooth	1.515	0.333	1.642	1 314	1 579
Sm-2	Smooth	1.520	0.333	1.655	1 319	1 595
Sm-3	Smooth	1.520	0.333	1.632	1 310	1 571
R20-1	2.0	1.534	0.658	1.018	1 206	1 012
R20-2	2.0	1.538	0.659	1.123	1 209	1 059
R20-3	2.0	1.539	0.659	1.084	1 209	1 017
R08-1	0.8	1.520	1.001	0.762	1 205	820
R08-2	0.8	1.523	1.002	0.761	1 187	739
R08-3	0.8	1.522	1.002	0.792	1 213	821

Fig. 5: Notched specimens called D1 and D2 (left and right respectively) used in compression-tension tests, with measures in mm.

since the D1 samples compressed to 0.60 failed in the threads during tension rather than in the initially notched area as this area became widest due to the compression. A summary of these material tests is given in Table 2, and additional details can be found in [4].

True stress-true strain curves for both specimen geometries are presented in Fig. 6. The scatter between the two parallel tests for D1 was very low. For the D2 series the scatter was
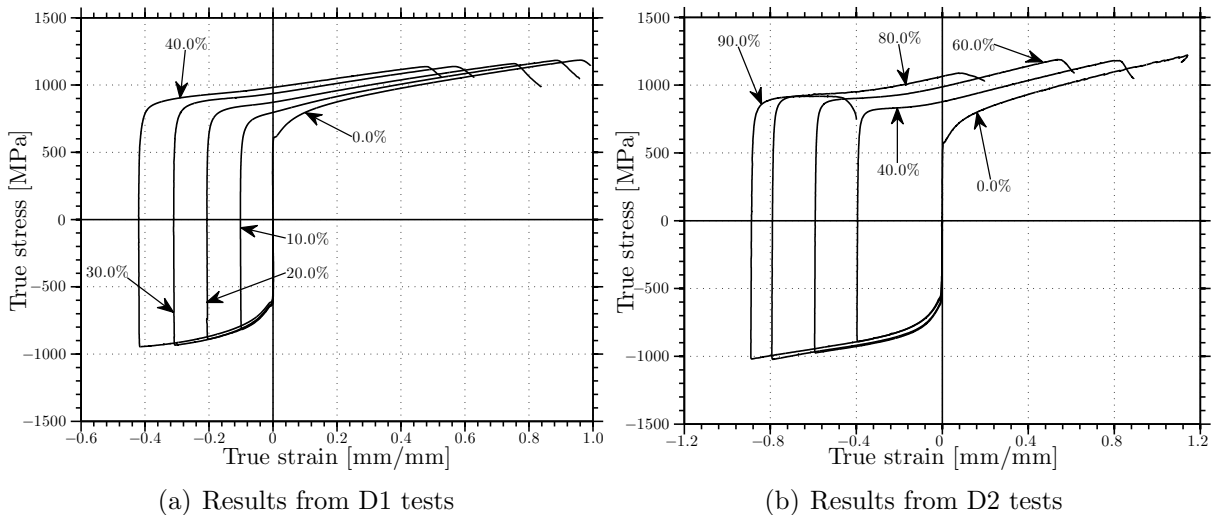

(a) Results from D1 tests   (b) Results from D2 tests

Fig. 6: True stress-true strain curves from compression-tension tests. Note the different abscissa.

7

Table 2: Summary of notched compression-tension tests.

Geometry	Comp.	ε_f	ε_r	$\varepsilon_{\mathrm{acc}}$	σ^*_{init}	$\hat{W}_{\mathrm{cr}}$ [MPa]	W_{cr} [MPa]
D1	0.0	0.96	0.96	0.96	0.701	991	991
	0.0	0.96	0.96	0.96	0.701	949	949
	0.10	0.87	0.97	1.07	-0.701	1053	976
	0.10	0.89	0.99	1.09	-0.701	1048	972
	0.20	0.75	0.95	1.16	-0.701	1105	944
	0.20	0.76	0.96	1.17	-0.701	1110	947
	0.30	0.54	0.85	1.16	-0.701	1107	849
	0.30	0.57	0.87	1.19	-0.701	1126	866
	0.40	0.43	0.84	1.27	-0.701	1224	864
	0.40	0.49	0.89	1.32	-0.701	1156	901
D2	0.0	1.14	1.14	1.14	0.578	1142	1142
	0.40	0.83	1.23	1.63	-0.578	1618	1282
	0.40	0.82	1.22	1.61	-0.578	1565	1252
	0.60	0.53	1.13	1.72	-0.578	1675	1173
	0.60	0.54	1.14	1.72	-0.578	1726	1209
	0.80	0.12	0.92	1.70	-0.578	1708	1015
	0.80	0.08	0.88	1.66	-0.578	1676	966
	0.90	-0.31	0.59	1.46	-0.578	1439	618
	0.90	-0.48	0.42	1.18	-0.578	1216	430

low as well, with the exception of the specimens compressed to 0.90 in which the fracture mode was altered from a typical cup-and-cone fracture to a 45° shear fracture as seen in Fig. 7. Similar results were also observed by Drucker et al. [6]. Further, the stress-strain curves in Fig. 6 have a "flat" part right after re-yielding, called work-hardening stagnation, also observed by several others [43, 44]. This can be explained by dislocations piling up around obstacles during compression, and when the load is reversed these dislocations experience less resistance when moving in the opposite direction [45].
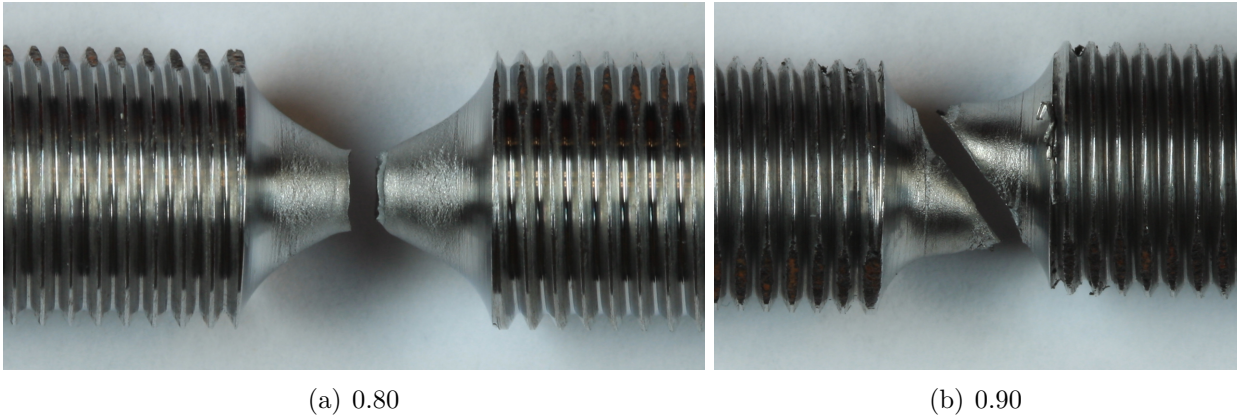

(a) 0.80   (b) 0.90

Fig. 7: Altered fracture mode between 0.80 and 0.90 compression strain before tension [4].

It is seen from Table 2 that the absolute fracture strain $\varepsilon_f = \ln(A_0/A_f)$ decreases with increasing compression, as does the relative fracture strain $\varepsilon_r = \ln(A_r/A_f)$ which arises from using the cross-sectional area at load reversal A_r as reference rather than the initial area A_0. A slight increase in the relative fracture strain is observed for compression to 0.10 true strain, as also noted by [33]. Table 2 also lists W_{cr} from Eq. (3), which decreases as the fraction of the tests where σ_1 is positive decreases. $\hat{W}_{cr}$ is calculated by replacing $\langle \sigma_1 \rangle$ with σ_1 in Eq. (3), which means that the contribution during compression is included. This value generally increases as the total "distance" the force acts on the specimen increases, which is quantified by the "accumulated" strain $\varepsilon_{acc} = \int \text{sgn}(\sigma_1) d\varepsilon^p$ along the entire load path. This measure also increases for increasing compression. An exception can be made for the highest compression levels (0.80 and above) as a transition is made to more cleavage fracture. The specimens fractured in a different mode for 0.90 compression as seen in Fig. 7. Scatter tends to increase with increasing compression, so some statistical consideration of the Beremin-type [46] could be a viable approach to model this in future studies.

Between D1 and D2 there is one overlapping compression level, which is 0.40. Inserting the two different radii $a_{D1} = 3.2$ mm and $a_{D2} = 2.0$ mm into Eq. (2), shows that the initial stress triaxiality for D2 is lower. Based on the results from Fig. 4(b) a lower fracture strain is expected for the D1 geometry, which is the case as listed in Table 2 and also confirmed by the D2-00 specimen.

In addition, reversed-loading tests at lower strains have been carried out to assess the amount of kinematic hardening [39]. This data has been used to calibrate the material model described in Section 3.

2.4. Metallurgy

From the component tests carried out by Kristoffersen et al. [4], cleavage fracture surfaces and cracked particles were observed in the area where compression had preceded tension. Particles cracked due to plastic straining can extend the cracks into the matrix, thereby initiating cleavage fracture [14]. When comparing 0.0 compression with 0.40, the latter seemed to result in more shallow and less elongated pores as seen in Fig. 8(a) and (b), and also observed in Al2024-T351 by Bao and Treitler [47]. This indicates reduced ductility [48].
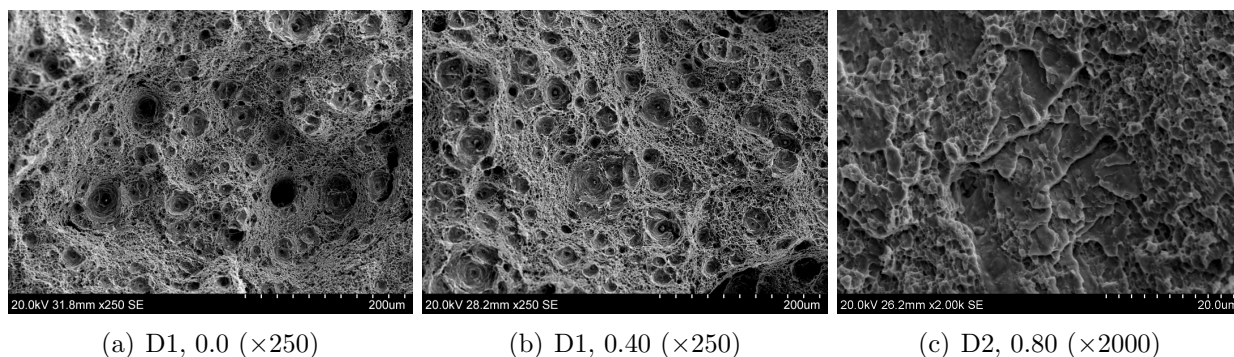

(a) D1, 0.0 (×250)   (b) D1, 0.40 (×250)   (c) D2, 0.80 (×2000)

Fig. 8: Fracture surfaces from specimens compressed to various levels and subsequently stretched to failure.

9

Cleavage fracture as observed in the pipe impact tests in [4] was recreated by the compression-tension material tests described above. While the lower compression values (≤ 0.40) mainly produced ductile fracture surfaces, the higher (0.60 and 0.80) managed to generate cleavage fracture, an example of which is shown in Fig. 8(c) for the 0.80 specimen. The 0.40 specimens did show signs of cleavage at the edges of the fracture surfaces. For the 0.90 specimens the fracture mode was as mentioned altered, which also changed the nature of the fracture surface to a combination of cleavage and directional pores typical of tearing. The main conclusions are that large scale plasticity can precede brittle fracture, and that compression-tension loading may induce a ductile-to-brittle transition. Unit cell simulations of compression-tension loading to large compressive strain are therefore carried out herein to see if they can provide some insight to which factors may contribute to the different fracture mechanisms.

3. Material model

3.1. Description

The elastic properties of the material are considered isotropic and linear, with Young's modulus E and Poisson ratio ν. Next, the yield function f describes the elastic domain in stress space with a combined isotropic and kinematic hardening law, and is given by

$$f\left(\boldsymbol{\sigma}, \boldsymbol{\chi}, R_H\right) = \sigma_{\mathrm{eq}}\left(\boldsymbol{\sigma} - \boldsymbol{\chi}\right) - \left(\sigma_0 + R_H\right) \leq 0 \tag{4}$$

in which σ_0 is the initial yield stress and R_H is the isotropic hardening variable. The von Mises equivalent stress σ_{eq} is a function of the deviatoric parts of the Cauchy stress tensor $\boldsymbol{\sigma}$ and the backstress tensor $\boldsymbol{\chi}$,

$$\sigma_{\mathrm{eq}}\left(\boldsymbol{\sigma} - \boldsymbol{\chi}\right) = \sqrt{\frac{3}{2}\left(\boldsymbol{\sigma}^{\mathrm{dev}} - \boldsymbol{\chi}^{\mathrm{dev}}\right) : \left(\boldsymbol{\sigma}^{\mathrm{dev}} - \boldsymbol{\chi}^{\mathrm{dev}}\right)} \tag{5}$$

Kinematic hardening is accounted for by the backstress $\boldsymbol{\chi}$, which defines the center of the elastic region. The tensor $\boldsymbol{\chi}$ and its evolution are described by the Armstrong-Frederick relation [49],

$$\boldsymbol{\chi} = \sum_{i=1}^{N_\chi} \boldsymbol{\chi}_i \ , \qquad \mathrm{d}\boldsymbol{\chi}_i = \frac{C_i}{\sigma_0 + R_H}\left(\boldsymbol{\sigma} - \boldsymbol{\chi}\right)\mathrm{d}\varepsilon_{\mathrm{eq}}^p - \gamma_i \boldsymbol{\chi}_i \mathrm{d}\varepsilon_{\mathrm{eq}}^p \tag{6}$$

where C_i and γ_i are material constants, N_χ is the number of backstresses, and R_H is a function of the accumulated equivalent plastic strain $\varepsilon_{\mathrm{eq}}^p$, given by

$$R_H\left(\varepsilon_{\mathrm{eq}}^p\right) = \sum_{j=1}^{N_V} Q_j \left[1 - \exp\left(-b_j \varepsilon_{\mathrm{eq}}^p\right)\right] \tag{7}$$

Eq. (7) is the Voce hardening law [50], in which Q_j and b_j are material constants, and N_V the number of terms included.

The associated flow rule defines the evolution of the plastic strain increment tensor $\mathrm{d}\boldsymbol{\varepsilon}^p$,
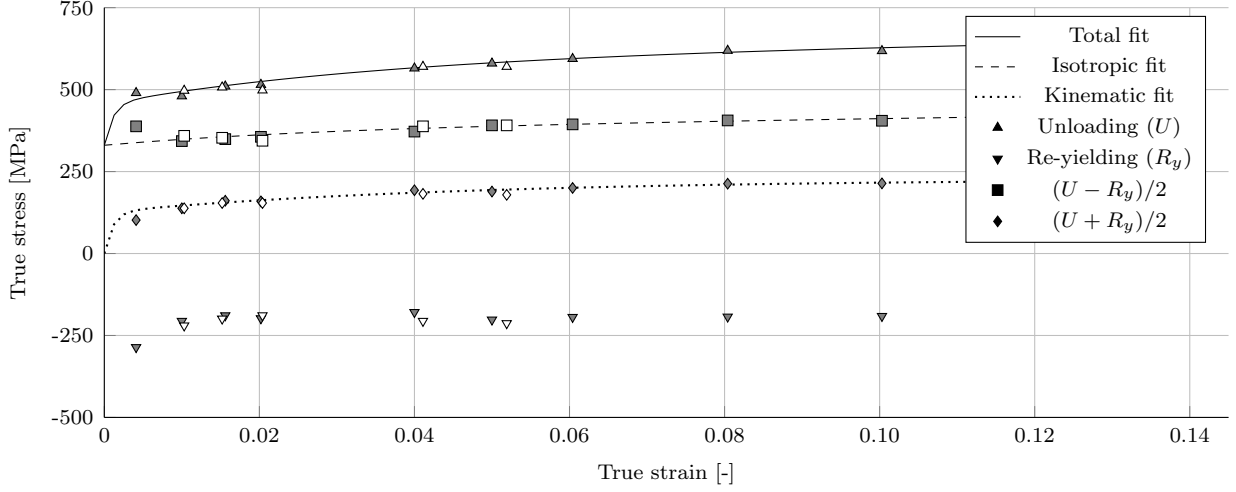
10

Fig. 9: Data used for calibration of the combined material model. The gray hatched markers are data from tension-compression tests while the white markers are for compression first (multiplied by −1). The solid line shows the combined fitted curve, the dashed line the isotropic part and the dotted line the kinematic part (the center of the elastic domain).

$$\mathrm{d}\boldsymbol{\varepsilon}^p = \mathrm{d}\lambda \cdot \frac{\partial f}{\partial\left(\boldsymbol{\sigma} - \boldsymbol{\chi}\right)} \tag{8}$$

where $\mathrm{d}\lambda \geq 0$ is the plastic parameter, and is equal to the scalar $\mathrm{d}\varepsilon^p_{\mathrm{eq}}$. The accumulated plastic strain $\varepsilon^p_{\mathrm{eq}}$ is obtained by integration,

$$\varepsilon^p_{\mathrm{eq}} = \int \mathrm{d}\varepsilon^p_{\mathrm{eq}} = \int \mathrm{d}\lambda \tag{9}$$

which amounts to summation of each plastic increment.

3.2. Calibration

To determine the flow stress σ_F after necking from the measured major principal stress σ_1 in Fig. 4(b), Bridgman's analysis [41] was employed

$$\sigma_F = \frac{\sigma_1}{\left(1 + \frac{2r}{a}\right) \cdot \ln\left(1 + \frac{a}{2r}\right)} \tag{10}$$

The relation between the radius of the specimen's cross-section at the root of the neck, a, and the radius of the neck profile, r, was estimated by the empirical relation proposed by Le Roy et al. [51]

$$\frac{a}{r} = 1.1 \cdot \left(\varepsilon^p_{\mathrm{eq}} - \varepsilon_U\right) \tag{11}$$

valid for $\varepsilon^p_{\mathrm{eq}} > \varepsilon_U$ where ε_U is the accumulated plastic strain at the onset of necking. When identifying the material constants, a least squares approximation [52] has been used to minimise the error.

11

Table 3: Constants for material model.

Elasticity and density		
E [MPa]	ν [-]	ρ [kg/m^3]
208 000	0.3	7 800

Combined model					
Isotropic	σ_0 [MPa] 330.3	Q_1 [MPa] 703.6	b_1 [-] 0.47	Q_2 [MPa] 50.5	b_2 [-] 34.7
Kinematic		C_1 [MPa] 115 640	γ_1 [-] 916	C_2 [MPa] 2 225	γ_2 [-] 22

The fraction of isotropic versus kinematic hardening can be estimated by calculating the size of the elastic domain from the reversed loading material tests in [39], a summary of which can be found in Fig. 9. The center of the elastic region is given by the point of unloading U and the point of re-yielding R_y, and it is calculated by $(U + R_y)/2$. Further, the size of the elastic domain is given by $(U - R_y)/2$.

From 0.20 plastic strain and upwards until failure, data points from the initial smooth uniaxial tesile tests were used. This results in isotropic hardening dominating the upper part of the strain levels. Two terms were used in both the isotropic and kinematic hardening parts, and the material constants (listed in Table 3) were fitted in a least squares sense as indicated earlier. For additional details, see [53]. Results of axisymmetric finite element simulations (described in Section 4) of the material tests from Fig. 4 using the calibrated material model can be seen in Fig. 10(a), and the fit was found to be good for all cases.

4. Global simulations

The global simulations concern the uniaxial tension tests whose geometries and results are shown in Fig. 4, and the compression-tension tests using the D1 and D2 geometries from Fig. 5, with adhering results plotted in Fig. 6. Stresses and strains from the global analyses are denoted σ and ε, respectively, with various sub- and superscripts. The simulations are run to validate the material model, and to extract triaxialities which will be applied to the unit cells in Section 5.

4.1. Setup

As the material is isotropic and the material test specimens are axisymmetric, the finite element simulations of the material tests are also made axisymmetric. Also, the symmetry line across the center of the specimen is exploited. The tension tests with geometries shown in Fig. 4(a) are modelled, as are the D1 and D2 compression-tension specimens displayed in Fig. 5. Like in the experiments, the loading is applied by deformation control until a prescribed level of plastic strain measured by change in cross-sectional area (i.e. diameter)

as expressed in Eq. (1) is obtained. All simulations herein are run with ABAQUS [54], and for the material tests the procedure is static and solved by a displacement-controlled Newton-Raphson procedure.

Four-node axisymmetric elements with reduced integration and hourglass control are used, and the elements are called `CAX4R` in ABAQUS. Five different mesh grades are examined, specified by the number of elements across the radius. The numbers chosen are 5, 10, 20, 50 and 100 elements for all specimen geometries. Results are plotted for the mesh with 20 elements across the radius.

4.2. Results

Results from the tension only simulations are plotted in Fig. 10(a) along with the experimental data, and these values are averages over the cross-section. As seen, the match is quite good for all three specimen geometries, at least for true strain values up to 1.0. The accuracy could be improved by performing an inverse modelling for the material parameters, but the accuracy is deemed sufficient for the current purpose. All mesh grades were able to reproduce the global response curves accurately, with the exception of the coarsest mesh which was a bit too stiff in the latter part of the simulations. In Fig. 10(b), the stress triaxiality σ^* at the center element is plotted versus the strain along the axis of symmetry ε_{33} in the same element. It is observed that for the two notched geometries, the triaxiality is fairly constant through the analysis whereas the smooth specimen has quite large variation – from about 1/3 in the beginning to above 1 at the end. The average triaxiality values are later used as boundary conditions for the unit cell analyses, and the accuracy is thus expected to be higher for the tests where the triaxiality has less variation.

The results are also good for the D1 specimens. However, as seen in Fig. 11(a), the work-hardening stagnation of the true stress-true strain curves after re-yielding is not optimally captured, overestimating the flow stress. This behaviour is difficult to predict with a few
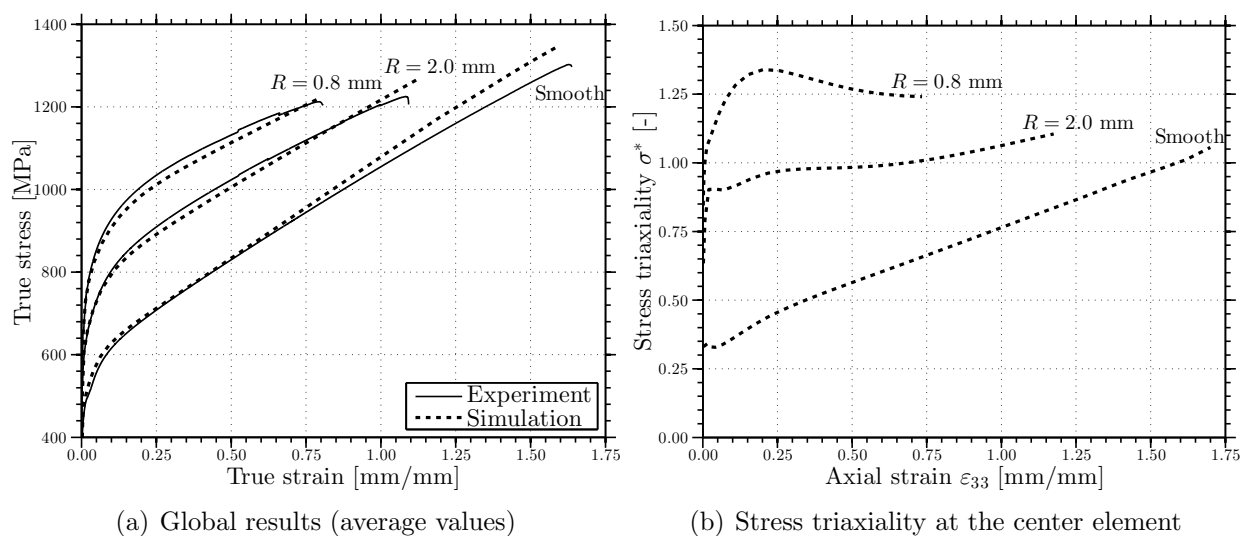

(a) Global results (average values)

(b) Stress triaxiality at the center element

Fig. 10: Results from finite element simulations of tension tests.

13

(a) Global results for D1

(b) Global results for D2

(c) Stress triaxiality at center element of D1
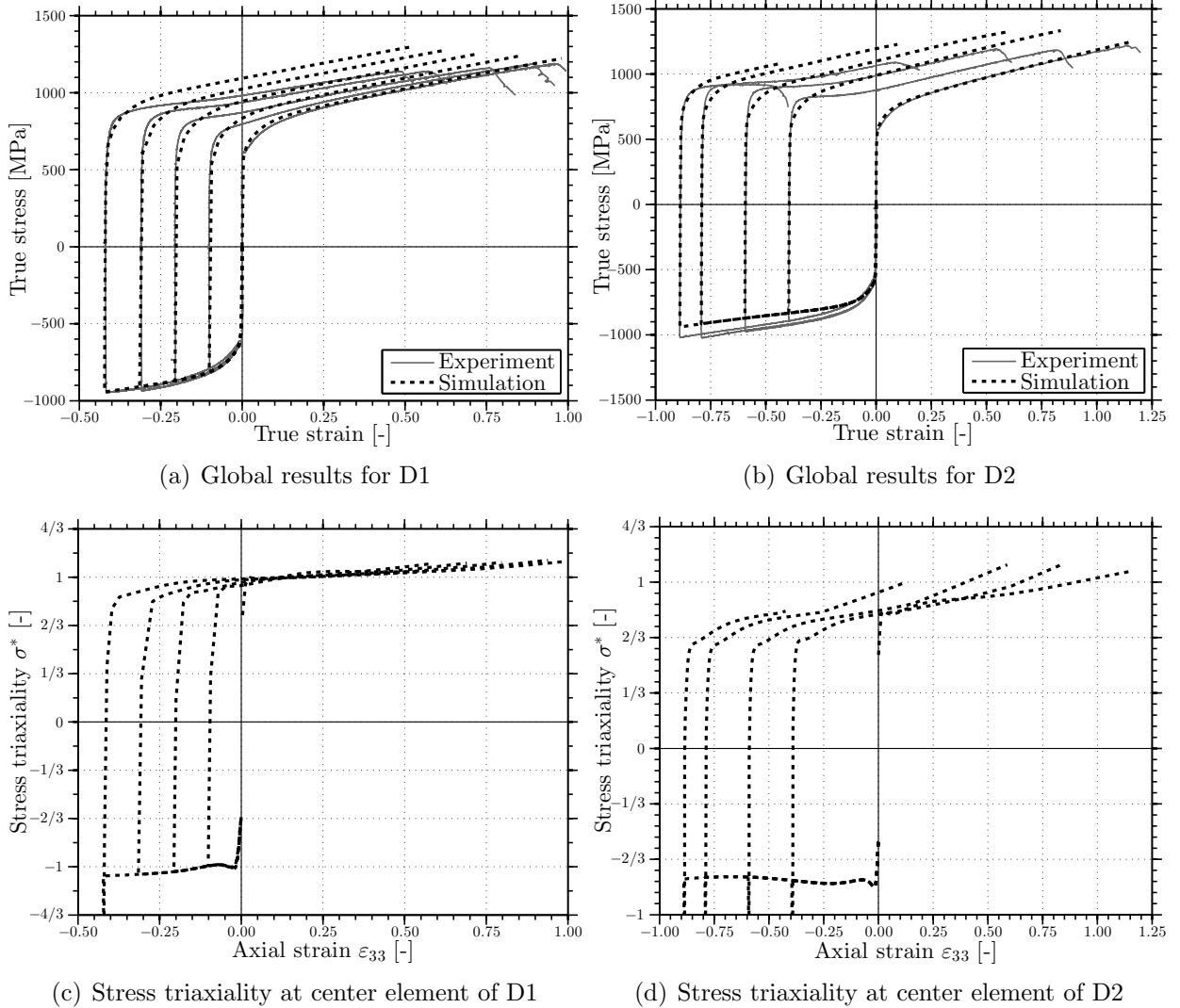
(d) Stress triaxiality at center element of D2

Fig. 11: Results from finite element simulations of compression-tension tests for both D1 and D2.

analytical expressions, and the material model's kinematic hardening part was calibrated for smaller strains than seen here. Higher estimated flow stress may lead to an inaccuracy when estimating the triaxiality at the center of the specimen, and hence a slight misrepresentation of the strain to failure later. Extending the model to include the work-hardening stagnation [33, 55] could provide better results, but this is beyond the scope of the present study. Similar judgement is cast upon the results for the D2 specimens in Fig. 11(b), which can also be said to be quite satisfactory for the current purpose. Stress levels for high compressive strains are slightly underestimated, while the stress levels during reversed loading in tension overestimate the experimental result. Like for the tension tests, triaxiality values will be extracted from the element in the center, where fracture is assumed to initiate.

From Fig. 11(c) it is observed that the compressive triaxiality is fairly constant at about

-1 for the D1 specimen. For the D2 specimens it also quite constant, but at a value of approximately -0.8 as can be seen in Fig. 11(d). The "spike" seen at the reversal point of some of the curves occurs due to moving through the elastic domain and thereby getting a very low magnitude of the equivalent stress, causing the artificial peak in negative triaxiality. These points are excluded when calculating the average triaxiality. In the D1 analyses, the triaxiality during tension has a slightly larger variation compared with the compression step – from a bit above 0.8 to just above 1.0. Due a larger relative change of geometry during testing, the variation is larger for the D2 samples, from about 0.6 to above 1.0. As the unit cells (described later) are subjected to a constant triaxiality, this may cause some inaccurate predicitons. In addition to using the average triaxialities from the tests, some chosen compressive triaxialities ($-1/3$, $-2/3$, -1, $-4/3$ and -2) will also be tested to assess the effect of using different triaxiality ratios during compression.

5. Unit cell simulations

Unit cell simulations with constant stress triaxialities have been run in an attempt to uncover potential features which may contribute to cleavage fracture. The triaxialities applied to the unit cells were estimated by the global simulations in the preceding section, and both tension-only loading as well as compression-tension loading is included. In addition, selected compressive triaxialities have been applied.

5.1. Setup

The unit cells are loaded with constant triaxiality, and stacked periodically in an approximate manner as described by Koplik and Needleman [16]. The x_3-axis in Fig. 12(a) is the axisymmetric axis, while the x_1-axis is a reflective axis of symmetry, limiting the model to one quadrant of the unit cell. Fig. 12(b) shows an example mesh of the quadrant in its initial state (top) and compressed state (bottom). Further, the cell is comprised of a hard spherical particle (linear elastic) and an elasto-plastic matrix material as described in Section 3. No cohesion between these two constituents is modelled, as the bonding between the two was found to be weak [4]. Fleck et al. [56] showed that including the contact in the particle/matrix interaction is important, especially at negative triaxialities, so contact was included by the penalty method and a coefficient of friction was chosen as $\mu = 0.4$. A parameter study on friction was run with coefficients ranging from 0.4 to 0.8, between which there were no significant differences. Any dependency on the Lode parameter is not investigated in the current study as all the simulations are axisymmetric, although the Lode effect can be significant [18]. It is possible to extend these kinds of simulations to 3D and more general load cases [19, 22, 23]. The initial particle volume fraction is denoted ω_0, and the combined void/particle volume fraction during deformation is designated ω.

Fig. 12(a) shows a cross-section through the center of the cylindrical cell, which has initial height $2H_0$ and initial radius R_0. One quadrant is then modelled axisymmetrically, and meshed as shown in Fig. 12(b) where the left edge is the axis of symmetry. The bottom edge is a mirror symmetry line, while the right and top edges are the edges to which the load is applied. The nodes on the top edge are restrained to having the same vertical deformation

15

(a) Axisymmetric unit cell quadrant   (b) Initial (top) and compressed mesh
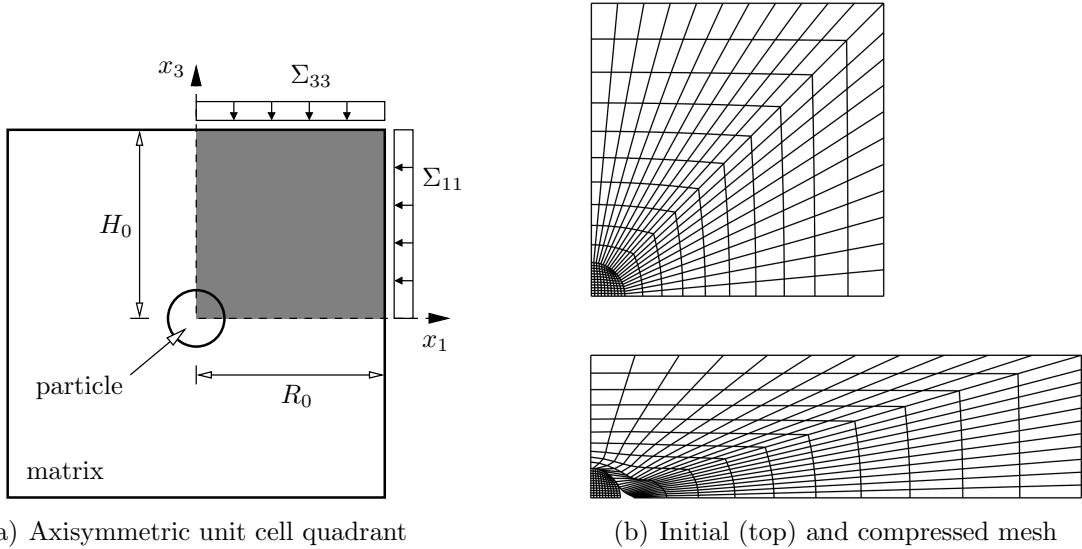
Fig. 12: One quadrant (hatched area) of unit cell (a) and the finite element mesh of said quadrant with particle and matrix (b), where the top part is the initial mesh and the bottom part a compressed mesh.

as the corner node, thereby keeping the top edge horizontal at all times. For the nodes on the lateral edge, the same principle is applied to keep that edge vertical. Again, axisymmetric elements of type `CAX4R` in ABAQUS [54] are used, which is a 4-node bilinear element with reduced integration and hourglass control. A brief mesh sensitivity study similar to that in the above section was run to find a fair compromise between accuracy and CPU time. 5, 10, 20, 50 and 100 elements across the particle and the matrix were tested, and the mesh in Fig. 12(b) (10 across) performed well in terms of both accuracy and CPU time. In addition no convergence issues were encountered with this mesh. The mesh with 5 elements across the particle and the matrix was the only one that deviated notably from the others by having a too stiff response.

The mesoscopic principal strains E_{11} and E_{33}, and the effective strain E_e, over the cell are defined by the current height H_c and current radius R_c of the cell [16],

$$E_{11} = \ln\left(\frac{R_c}{R_0}\right), \qquad E_{33} = \ln\left(\frac{H_c}{H_0}\right), \qquad E_e = \frac{2}{3}\left|E_{33} - E_{11}\right| \tag{12}$$

Similarly, from axisymmetry, the hydrostatic stress Σ_h and the von Mises effective stress Σ_e are given by

$$\Sigma_h = \frac{1}{3}\left(\Sigma_{33} + 2\Sigma_{11}\right), \qquad \Sigma_e = \left|\Sigma_{33} - \Sigma_{11}\right| \tag{13}$$

where Σ_{33} and Σ_{11} are the stresses in the axial and radial directions, respectively. Also, Σ_{22} is the tangential stress which is equal to Σ_{11} due to axisymmetry. The stress triaxiality ratio Σ^* over the cell is then defined by

$$\Sigma^* = \frac{\Sigma_h}{\Sigma_e} = \operatorname{sgn}(\Sigma_{33}) \cdot \frac{1 + 2\Sigma_c}{3\,|1 - \Sigma_c|} \tag{14}$$

in which Σ_c is the ratio of the mesoscopic stresses over the cell, i.e. $\Sigma_c = \Sigma_{11}/\Sigma_{33}$. The ratio has been extracted from the center element of the specimens from the global simulations carried out in Section 4, and then used when applying the loads Σ_{11} and Σ_{33} on the right and top edges (see Fig. 12(a)) as a uniform pressure. Both the tension tests and the compression-tension tests were used.

The unit cell analyses are driven by the Riks arc-length method [57] as implemented in ABAQUS [54]. A global load proportionality factor is increased incrementally to propagate the analyses forward, which means that the applied loads Σ_{11} and Σ_{33} are always scaled by the same factor, thus keeping the ratio Σ_c (and thereby the triaxiality) constant at all times throughout the analyses. This means that the compression-tension analyses, where the triaxiality changes when the load is reversed, have to be run in two steps where the compressive triaxiality is applied in one step and the tensile in the following step.

Further, the termination criterion for when the load is reversed is determined by the global analyses. The axial strain ε_{33} at maximum compression from the center element in the global analyses in Section 4 is used to calculate a deformation H_r at which the compression step ceases and the tension step commences,

$$H_r = H_0 \cdot \exp(\varepsilon_{33}) \tag{15}$$

based on E_{33} from Eq. (12). All three tension test triaxialities (smooth, $R = 2.0$ mm, and $R = 0.8$ mm) will be tested, and one case from each of the D1 and D2 specimens are chosen – namely the D1-40 specimen and the D2-80 specimen. Like in Section 2, the terms "absolute" strain to failure E_f and a "relative" strain to failure E_r will be used for the unit cells. The strain to failure is defined as the strain at which the stress drops suddenly[1] (see Fig. 13 for an example), where E_f uses the initial geometry as reference and E_r uses the geometry at load reversal. As the axial values E_{33} are the ones mainly discussed (explained later), they are also used for the strain to failure definitions – $E_f = \ln(H_f/H_0)$ and $E_r = \ln(H_f/H_r)$ where H_f is the height of the cell when the stress plummets. Table 4 lists both experimental and numerical values of both.

5.2. Results

First, the average triaxialities from the curves in Fig. 10(b) are applied to one unit cell each, with an experimentally determined initial particle volume fraction of $\omega_0 = 0.0005$. As anticipated, the average triaxiality $\overline{\Sigma}^*_{\text{smooth}} = 0.596$ from the smooth specimen geometry does not predict coalescence at the experimental strain level, or any other strain level as the triaxiality is below 2/3 [58]. There is simply too much variation in the geometry during testing for the average value to have adequate predictive capabilities (see Table 4). For the

---

[1]An alternative and equivalent indentification of this point is when the void/particle volume fraction increases abruptly, which is the point of interligament necking or void coalescence.

notched tests, however, the predictions based on the unit cells are quite good as can be observed in Fig. 13 and in Table 4. The estimated strain to coalescence is clearly within the same order as the experimentally measured fracture strain. In these tests, the triaxiality remains somewhat at the same level and an average value represents the load with decent accuracy ($\overline{\Sigma}^*_{R=2.0} = 0.982$ and $\overline{\Sigma}^*_{R=0.8} = 1.224$). Table 4 contains all the average triaxialities from the global analyses, as well as estimated initial experimental values.

In Fig. 13 it is evident that the sudden drop in the stress level coincides with the sudden increase in void/particle volume fraction. This point is identified as the onset of void coalescence. Fig. 13(a) shows the effective values of the normalised stress and the strain over the cell, whereas part (b) shows the axial values. Since the effective values Σ_e and E_e are absolute values (see Eq. (12) and (13)), they are not particularly well suited to visualise a reversal of the load and strain paths. The axial values Σ_{33} and E_{33} are negative for compression and positive for tension, and are henceforth chosen as visual aid to illustrate the response of each unit cell analysis which has a compression-tension load sequence. An example of a compressed computational cell can be seen at the bottom of Fig. 12(b).

Next, the compressive and tensile triaxiality data from the D1 and D2 analyses in Fig. 11(c) and 11(d) are applied to unit cells, and the axial strain is, as described above, used to define the axial deformation at which the load is reversed. Fig. 14(a) shows the normalised axial stress vs. the axial strain, while part (b) shows the development of the void/particle volume fraction as function of the axial strain. The critical void volume fraction for each curve is signified by a diamond shaped marker, whereas the gray circular markers on the stress curves indicate the point of maximum stress, which can be indicative of the near-onset of coalescence. For the tension-only specimen (D1-00) the predicted strain to coalescence is quite accurate, as it is 0.96 in the experiment and about 0.91 for the unit cell as can
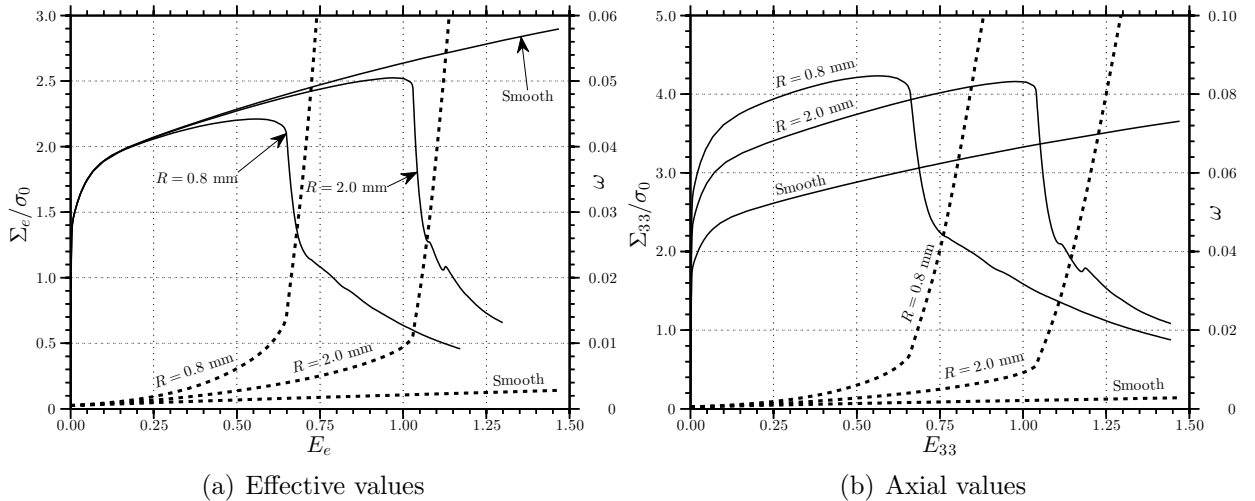

(a) Effective values   (b) Axial values

Fig. 13: Results from unit cell analyses using estimated average triaxialities from uniaxial tension tests. The solid lines show the stress normalised with respect to the calibrated yield stress (values on left axis in each subfigure) while the dotted lines indicate the void/particle volume fraction (values on right axis in each subfigure).

18

(a) Normalised axial stress

(b) Void/particle volume fraction

(c) Normalised axial stress
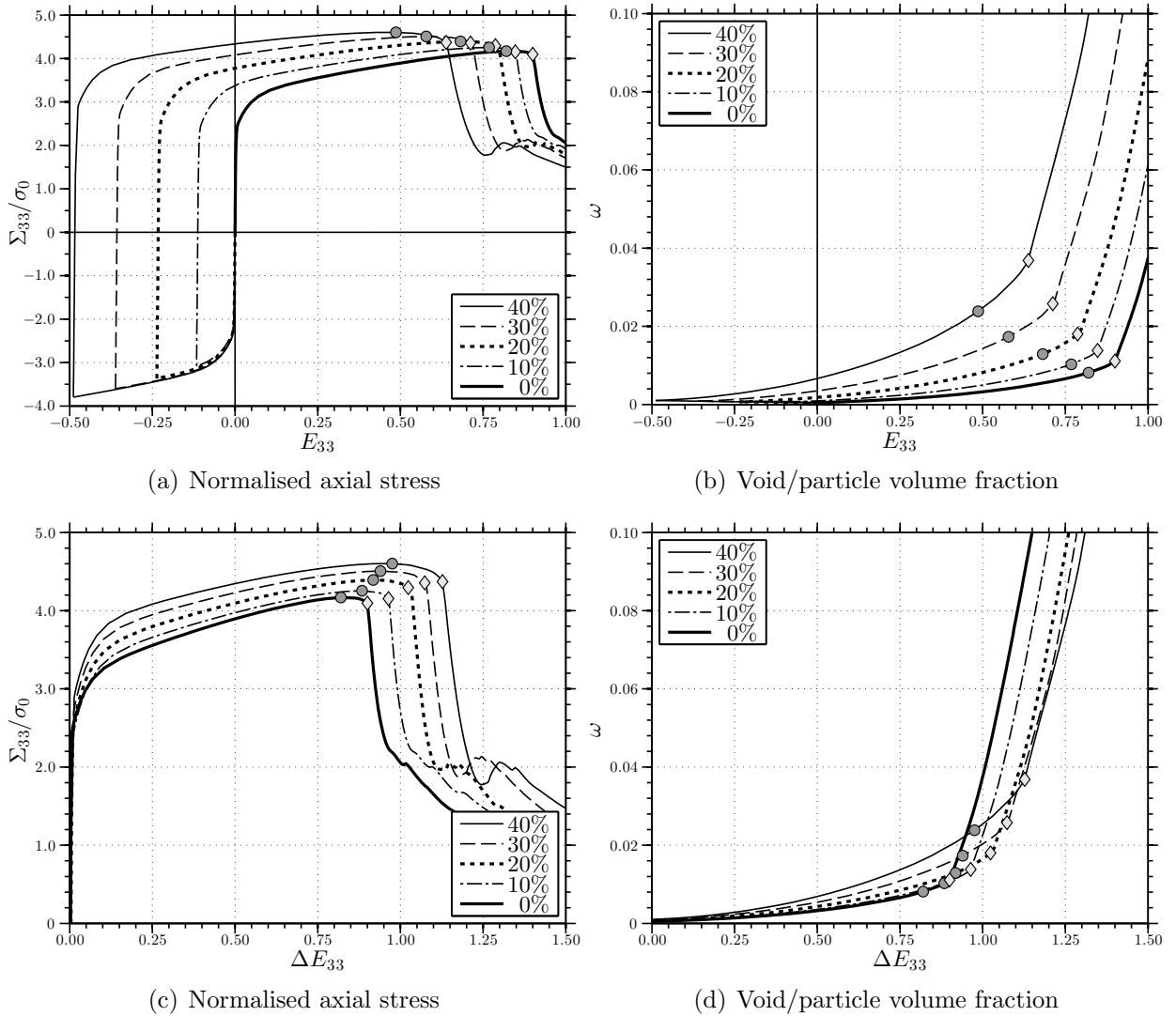
(d) Void/particle volume fraction

Fig. 14: Results from unit cell analyses with triaxiality data from global analyses of the D1 specimens. Parts (a) and (b) show the absolute strain values on the abscissa, while the abscissa in parts (c) and (d) show the relative strain from the point of load reversal for the tension step.

be seen in Table 4. The accuracy appears to diminish with increasing compression – the experimental absolute fracture strain was 0.46 for the D1-40 specimens, whereas the unit cell predicts 0.65. This indicates that some effects may not be adequately captured by the current unit cell model, e.g. the effect of having a non-constant stress triaxiality.

In Figs. 14(c) and (d) the resulting curves are translated to have the same origin for the tension load, thereby highlighting the relative strain ΔE_{33} after load reversal. As noted in Table 2, the relative fracture strain showed a decreasing trend with increasing compression before tension in the experiments. Quite the contrary is predicted by the unit cells – Fig. 14(c) shows an increased relative strain to coalescence E_r with increased compression (see Table 4 as well), along with an increase in the general stress level. Still, an accelerated

Table 4: Numerical estimates of strain to failure compared with average experimental values. $\overline{\Sigma}^*$ is the average triaxiality inferred from the global simulations and applied to the unit cell with the compressive triaxiality in parantheses, while E_f and E_r are the absolute and realative strains to failure, respectively.

	Numerical			Experimental		
Test	$\overline{\Sigma}^*$	E_r	E_f	σ^*_{init}	ε_r	ε_f
Smooth	(N/A) 0.596	N/A	-	0.333	N/A	1.61
R20	(N/A) 0.982	N/A	1.03	0.659	N/A	1.08
R08	(N/A) 1.224	N/A	0.67	1.002	N/A	0.77
D1-00	(N/A) 1.055	N/A	0.91	0.701	N/A	0.96
D1-10	(-0.947) 1.035	0.96	0.86	-0.701	0.98	0.88
D1-20	(-0.978) 1.021	1.03	0.80	-0.701	0.95	0.75
D1-30	(-1.002) 1.012	1.06	0.72	-0.701	0.86	0.55
D1-40	(-1.010) 1.000	1.10	0.65	-0.701	0.86	0.46
D2-00	(N/A) 0.908	N/A	1.20	0.578	N/A	1.14
D2-40	(-0.793) 0.840	1.57	1.08	-0.578	1.22	0.82
D2-60	(-0.787) 0.836	1.63	0.92	-0.578	1.13	0.53
D2-80	(-0.783) 0.810	1.84	0.87	-0.578	0.90	0.10
D2-90	(-0.782) 0.801	2.01	0.91	-0.578	0.50	-0.40

void growth after load reversal is observed when the compression is increased. Looking at Fig. 14(d) at e.g. $\Delta E_{33} = 0.75$, the void/particle volume fraction ω is about twice as large for D1-40 compared with D1-00. Nevertheless, coalescence occurs for a lower ΔE_{33} value and a lower ω value for the D1-00 case. Attaining the maximum stress also requires additional straining with increasing compression, and the maximum stress level increases with increasing compression.

The same observations are made when the analyses are extended to the D2 specimens, and the noted effects are amplified with higher compression values (see Fig. 15). Higher compression leads to an even more accelerated void growth, and seemingly delayed onset of coalescence. More interestingly, the point of maximum load appears to arrive earlier during tension when going beyond 0.40 compression as seen in Fig. 15(c). Further, Figs. 15(b) and 15(d) show that the point of maximum load occurs at similar levels of void volume fraction. In the D2 analyses, the maximum normalised axial stress during tension is virtually the same for all compression levels, while the D1 analyses had more variation (higher compression leads to higher maximum stress).

A separate study was conducted with triaxialities $\Sigma^*_{\text{comp}} = -1$ and $\Sigma^*_{\text{tens}} = 1$, where the unit cell was compressed to 0.0 (i.e. tension only), 0.20, 0.40, 0.60, 0.80 and 1.00. The results were quite similar to what is shown in Figs. 14 and 15, and are omitted for brevity.

Next, a few analyses are run to investigate the effect of how the magnitude of compressive (negative) triaxiality affects the subsequent tensile behaviour. The chosen values for the negative triaxialities Σ^*_{comp} are -2, $-4/3$, -1, $-2/3$ and $-1/3$, and the tensile triaxiality is selected to be the same for all analyses, $\Sigma^*_{\text{tens}} = 1$. As above, six compression levels from

(a) Normalised axial stress

(b) Void/particle volume fraction

(c) Normalised axial stress

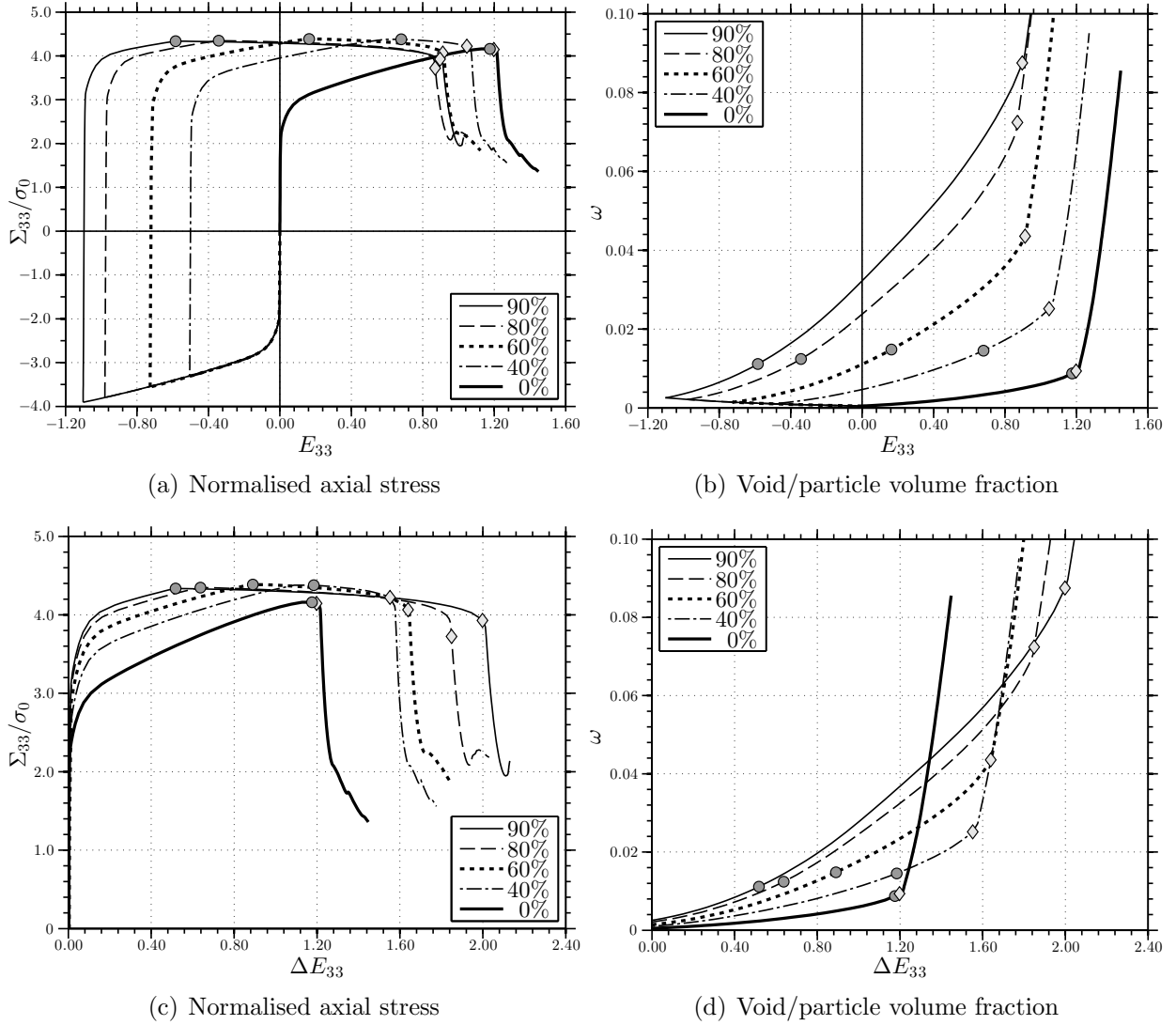(d) Void/particle volume fraction

Fig. 15: Results from unit cell analyses with triaxiality data from global analyses of the D2 specimens. Parts (a) and (b) show the absolute strain values on the abscissa, while the abscissa in parts (c) and (d) show the relative strain from the point of load reversal.

0.0 to 1.00 were chosen, and the analyses compressed to 0.20 and 0.80 are picked out to highlight the main results.

The most notable feature of changing the compressive triaxiality is that a higher magnitude results in a higher axial stress level in the cell during compression. It also produces a higher stress level during tension (even though $\Sigma^*_{\text{tens}} = 1$ for all cases) as Figs. 16(a) and 16(c) will attest to. The strain to coalescence (and to the point of maximum stress) is also reduced significantly when the compressive triaxiality increases in magnitude, in spite of the subsequent tensile triaxiality remaining the same. An accelerated void growth is also noted, as shown in Figs. 16(b) and 16(d). The void/particle volume fraction increases more

(a) Normalised axial stress (0.20)

(b) Void/particle volume fraction (0.20)

(c) Normalised axial stress (0.80)
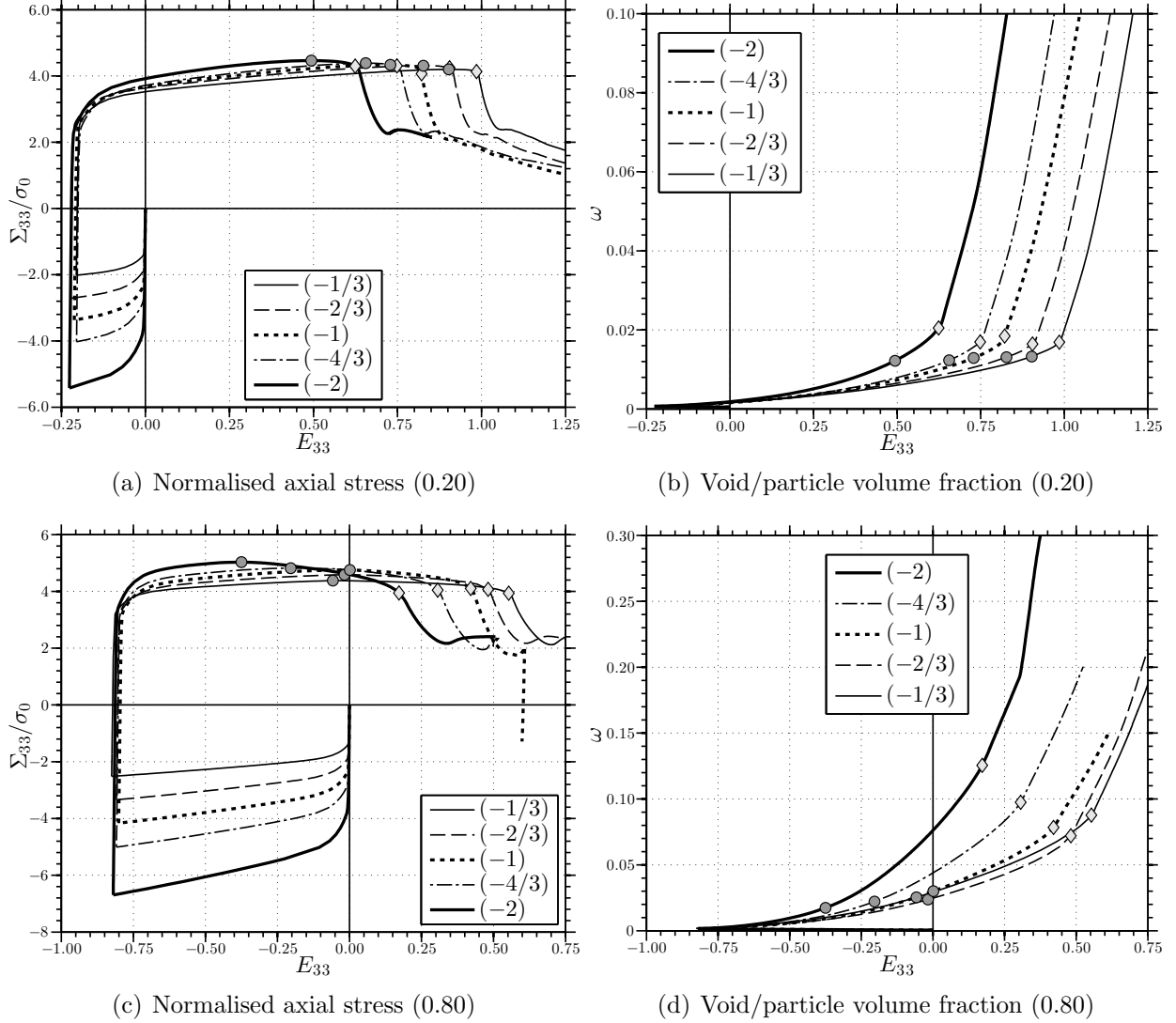
(d) Void/particle volume fraction (0.80)

Fig. 16: Results from unit cell analyses with specified triaxiality data and compression to 0.20 (top row) and to 0.80 (bottom row) before tension is applied until failure.

rapidly when the compressive triaxiality has had a higher magnitude. All these effects seem to be amplified by the level of compression. Where Fig. 16(b) shows a clear indication of the onset of coalescence for each curve, i.e. the sudden increase in void/particle volume fraction, Fig. 16(d) illustrates that this point becomes somewhat more ambiguous with increasing compression and increasing magnitude of compressive triaxiality. Again it is observed that the point of maximum load occurs at void volume fractions which are much alike.

In Fig. 17 the maximum principal stress (relative to the yield stress) locally in the unit cell after load reversal has been plotted vs. the compressive triaxiality. This local stress has been picked after a tensile strain increment of $\Delta E_{33} = 0.50$ has been applied, and this has been done for all compression levels run (0.0, 0.20, 0.40, 0.60, 0.80 and 1.00). Here
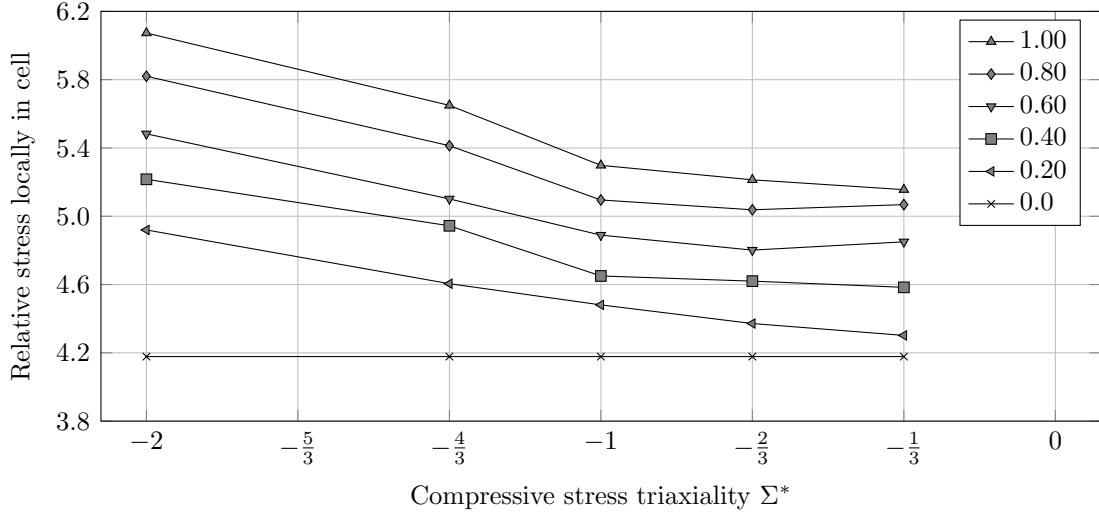
Fig. 17: Largest local main principal stress (relative to the yield stress) in unit cell vs. compressive triaxiality after a load sequence of compression to different levels (0.0, 0.20, 0.40, 0.60, 0.80 and 1.00) followed by a tensile strain of $\Delta E_{33} = 0.50$.

it is evident that increasing the compression level and increasing the magnitude of the compressive triaxiality, both clearly contribute to increasing the local maximum principal stress in the cell.

6. Discussion

Based on the uniaxial tension tests the material was characterised as homogeneous and isotropic. Notched tension tests showed that a sharper notch reduced the strain to failure. Tensile prestrain on X65 steel has been shown to have a negative effect on the strain to failure [59], while compressive prestrain on an X65 material has been shown to have a negative effect on the critical crack-tip opening displacement [8]. Compression-tension tests carried out by Kristoffersen et al. [4] showed that both the absolute and relative strains to fracture decreased with increasing compression, while Papasidero et al. [12] have reported an increase in ductility after precompressing dual phase steel sheets. Further, spherical particles with poor bonding to the matrix were discovered in relation with fracture. Voids typically nucleate due to particle-matrix decohesion and/or cracking of particles [60], which may occur during compression (illustrated by Sabih and Nemes [61]) and can thereby cause the observed decrease in tensile strain to failure after compression. The magnitude of the compressive strain is important, as higher compression leads to lower strain to failure in tension. For the lowest compression level (0.10 true strain), the subsequent tensile strain to failure increased slightly as seen in Table 2. This was also observed by Marcadet and Mohr [33], who compressed dual phase steel sheet specimens (up to 13%). Compression before tension can lead to particle failure and an increase in dislocation density [47], both of which can accelerate void nucleation and growth. Cracks in particles due to inhomogeneous plastic straining can propagate into the ferrite matrix [14]. Kweon [62] argues from a crystal

23

plasticity based model that damage at negative triaxiality occurs due to development of tensile hydrostatic stresses during grain-to-grain interaction, which may be the case in the D1 and D2 experiments along with cracking of particles and alignment of the grain boundaries during compression. These aligned boundaries may serve as preferred crack planes and thereby emerge as cleavage fracture when the load is reversed. Also, cleavage fracture was observed for the larger compressive values in [4], indicating that large scale plasticity may precede cleavage fracture as also noted by Smith [63]. Signs of local cleavage was also observed by Enami [9] after compression-tension loading.

Axisymmetric finite element analyses were run of the material tests, and the global results were quite accurate. The exception is the part of the true stress-true strain curve in the compression-tension tests right after re-yielding where work-hardening stagnation occurs. This behaviour can be somewhat difficult to capture accurately and would require more complex models [33, 55] for improved accuracy. Nevertheless, the overall response can be said to be satisfactory for the current use. These global analyses of the material tests were also used to provide triaxiality values for use with the subsequent unit cell analyses.

Constant stress triaxiality unit cell analyses with axisymmetric elements were run in ABAQUS, driven by a Riks-type [57] solution procedure with a global load proportionality factor. A combined isotropic/kinematic hardening model was used, which for nodular cast iron has been shown to perform better compared with pure isotropic or pure kinematic hardening [31]. The unit cell results based on tests where the triaxiality was fairly constant, which means primarily the notched tension tests, were encouraging and predicted the fracture strain with decent accuracy. The triaxiality from the smooth tension test had too much variation to be accurately represented by a constant triaxiality. The tension-only unit cell simulations showed results conforming with the multitude of studies already conducted with tension loading (see Benzerga and Leblond [58] for an excellent overview).

The triaxiality from the compression-tension tests were also quite constant, at least in the compression phase. Still, the strain to fracture after load reversal in the unit cell was not predicted with sufficient accuracy. Compression before tension accelerated the void growth during tension. Tensile prestrain has been shown to reduce the strain to void coalescence [24], and Vaz Jr et al. [30] showed that the strain path is important. For the D1 simulations, the strain increment to coalescence after load reversal increased with increasing compression, contrary to what was expected based on the experimental data. This means that the critical void volume fraction of the material could be decreased by increasing compression, or the precompression could trigger a different fracture mechanism. The same was observed for the D2 simulations but not for the point of maximum stress, which occured earlier after load reversal for the compression levels above 0.40, and at comparable levels of void volume fraction.

Further analyses were conducted with other compressive triaxiality values. These showed that increasing the magnitude of the triaxiality in compression leads to an increase in the stress level in the cell both during compression and in the subsequent tension, which had the same tensile stress triaxiality regardless of the compressive value. Increasing the magnitude of the compressive triaxiality also contributed to an accelerated void growth, earlier onset of coalescence, and earlier occurence of the peak load, effects which are all amplified by

24

increasing the level of compression, as seen in Fig. 16. Failure in the experiments typically occur between the point of maximum load and onset of coalescence in the simulations.

Unit cells are a useful tool in understanding the ductile fracture process, and can even give some insights regarding brittle fracture in terms of local stress concentrations. Ritchie et al. [29] argued that cleavage will occur when the stress exceeds a certain level over a critical distance, and with higher stress levels a criterion of this kind is a natural approach. A technique like this was employed by Gao et al. [64], who required the volume average of the stress over a cleavage grain to exceed a specified critical stress value, independent of strain rate and temperature. As properties like grain sizes and particles adhere to some statistical distribution, a statistical approach may be helpful [46, 65]. In any case, decent predictions were made for the tension tests with fairly constant triaxiality, whereas predicting fracture for reversed loading is somewhat more difficult. The stress at which the material failed in the tests was similar for most specimens, and the peak mesoscopic stress in most unit cell simulations was also of similar magnitude. Fig. 17 shows the increasing local stress in the unit cell – and the increase is due to both increasing level of compressive strain and increase in magnitude of triaxiality during compression. Any factor that increases the yield stress also increases the susceptibility to cleavage [34], and higher stress along with inhomogeneous plastic deformation can cause cleavage [63]. These observations argues for incorporating a stress based failure criterion, since such an approach would replicate the trends observed experimentally, demonstrated here by Fig. 17. A critical stress is a different mechanism than interligament necking, thereby necessitating a different approach. However, as also noted by Benzerga et al. [25], both the strain path and the history of stress triaxiality are important.

7. Conclusions

This work has investigated the axisymmetric compression-tension experiments on an X65 offshore material carried out by Kristoffersen et al. [4]. Simulations of the material tests and unit cell simulations have been conducted to examine the observed ductile-to-brittle transition. Based on the experimental work it can be said that the X65 material behaves isotropically, and that the pipe from which the specimens are taken is homogeneous across the cross-section [4]. A sharper notch (i.e. increased triaxiality) reduces the strain to failure, a result conforming with the unit cell simulations. It is observed that the load path is very important, and that large compressive strains before tension can reduce the subsequent tensile strain to failure. Particles may crack or debond from the matrix during compression, which may be the source of the observed reduction of failure strain. Alignment of grain boundaries can also contribute to this. The peak stress at which the material failed in the experiments was fairly constant.

The observations made have been further investigated using unit cell simulations, from which the following conclusions may be drawn:

- Constant-triaxiality axisymmetric unit cell simulations of the tension-only tests produce good estimates of the strain to failure, except for the smooth specimen where the triaxiality varies too much to be represented accurately by a constant triaxiality.

- The unit cell simulations predict increased failure strain for compression-tension loading despite showing an accelerated void growth during tension. The increased failure strain is contrary to the experimental data, which means that compression could lead to a decreased critical void volume fraction or trigger a different fracture mechanism.

- The strain to maximum load after load reversal decreases for compression levels above 0.40 strain. Failure in the experiments typically occurred between the point of maximum load and onset of coalescence in the simulations, and the point of maximum load may be used as a failure indicator. Further, it was found that maximum load occurs at similar levels of void volume fraction. A natural extension of the model would be to include a stress based criterion for failure.

- Increased magnitude of compressive triaxiality increases the magnitude of the stress in the cell – both during compression and the following tension despite that the tensile triaxiality was the same for all cases – thereby elevating the probaility of failure. A larger magnitude of triaxiality during compression also leads to an accelerated void growth and an earlier onset of void coalescence, in addition to making the peak stress occur earlier.

The current work has shown that unit cells remain a useful tool for qualitatively investigating the effect of stress state (and history thereof) on fracture. Even if some predicitons are not accurate, it is still possible to gain insight to the fracture process. Together with good experimental data, lower scale models are central to understanding material behaviour.

References

[1] N. Jones, Inelastic response of structures due to large impact and blast loadings, Journal of Strain Analysis for Engineering Design 45 (2010) 451–464.

[2] N. Jones, R. Birch, Influence of internal pressure on the impact behaviour of steel pipelines, International Journal of Pressure Vessel Technology 118 (1996) 464–471.

[3] M. Kristoffersen, T. Børvik, M. Langseth, O. Hopperstad, Dynamic versus quasi-static loading of X65 steel pipes, European Physical Journal – Special Topics 225 (2016) 325–334.

[4] M. Kristoffersen, T. Børvik, I. Westermann, M. Langseth, O. Hopperstad, Impact against X65 steel pipes — An experimental investigation, International Journal of Solids and Structures 50 (2013) 3430–3445.

[5] J. Ludley, D. Drucker, A Reversed-Bend Test to Study Ductile to Brittle Transition, Welding Journal (Research Supplements) 39 (1960) 543–546.

[6] D. Drucker, C. Mylonas, G. Lianis, Exhaustion of Ductility of E-Steel in Tension Following Compressive Prestrain, Welding Journal (Research Supplements) 39 (1960) 117–120.

[7] P. Eikrem, Z. Zhang, B. Nyhus, Effect of plastic prestrain on the crack tip constraint of pipeline steels, International Journal of Pressure Vessels and Piping 84 (2007) 708–715.

[8] N. Fukuda, N. Hagiwara, T. Masuda, Effect of Prestrain on Tensile and Fracture Toughness Properties of Line Pipes, Journal of Offshore Mechanics and Arctic Engineering 127 (2005) 263–268.

[9] K. Enami, The effects of compressive and tensile prestrain on ductile fracture initiation in steels, Engineering Fracture Mechanics 72 (2005) 1089–1105.

[10] P.-O. Bouchard, L. Bourgeon, H. Lachapele, E. Maire, C. Verdu, R. Forestier, R. Loge, On the influence of particle distribution and reverse loading on damage mechanisms of ductile steels, Materials Science and Engineering A 496 (2008) 223–233.

[11] Y. Bao, T. Wierzbicki, On fracture locus in the equivalent strain and stress triaxiality space, International Journal of Mechanical Sciences 46 (2004) 81–98.

[12] J. Papasidero, V. Doquet, D. Mohr, Ductile fracture of aluminum 2024-T351 under proportional and non-proportional multi-axial loading: Bao-Wierzbicki results revisited, International Journal of Solids and Structures 69-70 (2015) 459–474.

[13] D. Curry, J. Knott, Effects of microstructure on cleavage stress in steel, Metal Science 12 (1978) 511–514.

[14] C. McMahon, M. Cohen, Initiation of fracture in polycrystalline iron, Acta Metallurgica 13 (1965) 591–604.

[15] V. Tvergaard, Influence of voids on shear band instabilities under plane strain conditions, International Journal of Fracture 17 (1981) 389–407.

[16] J. Koplik, A. Needleman, Void growth and coalescence in porous plastic solids, International Journal of Solids and Structures 24 (1988) 835–853.

[17] R. Tian, S. Chan, S. Tang, A. Kopacz, J.-S. Wang, H.-J. Jou, L. Siad, L.-E. Lindgren, G. Olson, W. Liu, A multiresolution continuum simulation of the ductile fracture process, Journal of Mechanics and Physics of Solids 58 (2010) 1681–1700.

[18] I. Barsoum, J. Faleskog, Rupture mechanisms in combined tension and shear – Micromechanics, International Journal of Solids and Structures 44 (2007) 5481–5498.

[19] I. Barsoum, J. Faleskog, Micromechanical analysis on the influence of the Lode parameter on void growth and coalescence, International Journal of Solids and Structures 48 (2011) 925–938.

[20] F. Scheyvaerts, P. Onck, C. Tekoglu, T. Pardoen, The growth and coalescence of ellipsoidal voids in plane strain under combined shear and tension, Journal of the Mechanics and Physics of Solids 59 (2011) 373–397.

[21] M. Brünig, S. Gerke, V. Hagenbrock, Micro-mechanical studies on the effect of the stress triaxiality and the Lode parameter on ductile damage, International Journal of Plasticity 50 (2013) 49–65.

[22] C. Tekoglu, Representative volume element calculations under constant stress triaxiality, Lode parameter, and shear ratio, International Journal of Solids and Structures 51 (2014) 4544–4553.

[23] M. Dunand, D. Mohr, Effect of Lode parameter on plastic flow localisation after proportional loading at low stress triaxialities, Journal of the Mechanics and Physics of Solids 66 (2014) 133–153.

[24] Z. Zhang, B. Skallerud, Void coalescence with and without prestrain history, International Journal of Damage Mechanics 19 (2010) 153–174.

[25] A. Benzerga, D. Surovik, S. Keralavarma, On the path-dependence of the fracture locus in ductile materials – Analysis, International Journal of Plasticity 37 (2012) 157–170.

[26] D. Steglich, W. Brocks, Micromechanical modelling of the behaviour of ductile materials including particles, Computational Materials Science 9 (1997) 7–17.

[27] M. Kroon, J. Faleskog, Micromechanics of cleavage fracture initiation in ferritic steels by carbide cracking, Journal of the Mechanics and Physics of Solids 53 (2005) 171–196.

[28] G. Hütter, L. Zybell, M. Kuna, Micromechanical modeling of crack propagation in nodular cast iron with competing ductile and cleavage failure, Engineering Fracture Mechanics (2015). http://dx.doi.org/10.1016/j.engfracmech.2015.06.039.

[29] R. Ritchie, J. Knott, J. Rice, On the relationship between critical tensile stress and fracture toughness in mild steel, Journal of Mechanics and Physics of Solids 21 (1973) 395–410.

[30] M. Vaz Jr, N. de Santi Jr, E. de Souza Neto, Numerical Prediction of Ductile Failure Onset under Tensile and Compressive Stress States, International Journal of Damage Mechanics 19 (2010) 175–195.

[31] Rabold, F., Kuna, M., Cell model simulation of void growth in nodular cast iron under cyclic loading, Computational Materials Science 32 (2005) 489–497.

[32] F. Yoshida, T. Uemori, K. Fujiwara, Elastic-plastic behavior of steel sheets under in-plane cyclic tension-compression at large strain, International Journal of Plasticity 18 (2002) 633–659.

[33] S. Marcadet, D. Mohr, Effect of compression-tension loading reversal on the strain to fracture of dual phase steel sheets, International Journal of Plasticity 72 (2015) 21–43.

[34] T. Anderson, Fracture mechanics - Fundamentals and applications, third ed., Taylor and Francis Group, 2005.

[35] A. Pineau, Modeling ductile to brittle fracture transition in steels – micromechanical and physical challenges, International Journal of Fracture 150 (2008) 129–156.

[36] C.-K. Oh, Y.-J. Kim, J.-H. Baek, W.-S. Kim, Development of stress-modified fracture strain for ductile failure of API X65 steel, International Journal of Fracture 143 (2007) 119–133.

[37] M. Kristoffersen, F. Casadei, T. Børvik, M. Langseth, O. Hopperstad, Impact against empty and water-filled X65 steel pipes – Experiments and simulations, International Journal of Impact Engineering 71 (2014) 73–88.

[38] M. Kristoffersen, F. Casadei, T. Børvik, M. Langseth, G. Solomos, O. Hopperstad, Numerical simulations of submerged and pressurised X65 steel pipes, XII International Conference on Computational Plasticity, Barcelona, Spain (2013).

[39] M. Kristoffersen, T. Børvik, M. Langseth, H. Ilstad, E. Levold, O. Hopperstad, Damage and failure in an X65 steel pipeline caused by trawl gear impact, Proceedings of the ASME 2013 32nd International Conference on Ocean, Offshore and Arctic Engineering (2013).

[40] M. Fourmeau, T. Børvik, A. Benallal, O. Hopperstad, Anisotropic failure modes of high-strength aluminium alloy under various stress states, International Journal of Plasticity 48 (2013) 34–53.

[41] R. Hill, The Mathematical Theory of Plasticity, Oxford University Press, 1950.

[42] M. Cockcroft, D. Latham, Ductility and the workability of metals, Journal of the Institute of Metals 96 (1968) 33–39.

[43] C. Teodisu, Z. Hu, Evolution of intragranular microstructures at moderate and large strains: Modelling and computational significance, Simulation of Materials Processing: Theory, Methods and Applications (1995) 173–182.

[44] G. Vincze, E. Rauch, J. Gracio, F. Barlat, A. Lopes, A comparison of the mechanical behaviour of an AA1050 and a low carbon steel deformed upon strain reversal, Acta Materialia 53 (2005) 1005–1013.

[45] T. Hasegawa, T. Yakou, U. Kocks, Forward and Reverse Rearrangements of Dislocations in Tangled Walls, Materials Science and Engineering 81 (1986) 189–199.

[46] F. Beremin, A Local Criterion for Cleavage Fracture of a Nuclear Pressure Vessel Steel, Metallurgical Transactions A 14A (1983) 2277–2287.

[47] Y. Bao, R. Treitler, Ductile crack formation on notched Al2024-T351 bars under compression-tension loading, Materials Science and Engineering A 384 (2004) 385–394.

[48] R. Ghajar, G. Mirone, A. Keshavarz, Ductile failure of X100 pipeline steel – Experiments and fractography, Materials and Design 43 (2013) 513–525.

[49] P. Armstrong, C. Frederick, A mathematical representation of the multiaxial Bauschinger effect, Technical Report, G.E.G.B. Report RD/B/N731, 1966.

[50] E. Voce, The relationship between stress and strain for homogeneous deformation, Journal of the Institute of Metals 74 (1948) 536–562.

[51] G. Le Roy, J. Embury, M. Ashby, A model of ductile fracture based on the nucleation and growth of voids, Acta Metallurgica 29 (1981) 1509–1522.

[52] H. Anton, C. Rorres, Elementary linear algebra, ninth ed., John Wiley & Sons Inc., New York, 2005.

[53] M. Kristoffersen, Impact against X65 offshore pipelines, Ph.D. thesis, Norwegian University of Science and Technology, 2014.

[54] Abaqus analysis user's manual version 6.11, SIMULIA, 2013.

[55] F. Yoshida, T. Uemori, A model of large-strain cyclic plasticity describing the Bauschinger effect and workhardening stagnation, International Journal of Plasticity 18 (2002) 661–686.

[56] N. Fleck, J. Hutchinson, V. Tvergaard, Softening by void nucleation and growth in tension and shear, Journal of the Mechanics and Physics of Solids 37 (1989) 515–540.

[57] E. Riks, An incremental approach to the solution of snapping and buckling problems, International Journal of Solids and Structures 150 (1979) 529–551.

[58] A. Benzerga, J.-B. Leblond, Ductile fracture by Void Growth to Coalescence, Advances in Applied Mechanics 44 (2010) 174–304.

[59] C.-K. Oh, Y.-J. Kim, J.-H. Baek, Y.-P. Kim, W.-S. Kim, A phenomenological model of ductile fracture of API X65 steel, International Journal of Mechanical Sciences 49 (2007) 1399–1412.

[60] S. Goods, L. Brown, The nucleation of cavities by plastic deformation, Acta Metallurgica 27 (1979) 1–15.

[61] A. Sabih, J. Nemes, Internal ductile failure mechanisms in steel cold heading process, Journal of Materials Processing Technology 209 (2009) 4292–4311.

[62] S. Kweon, Damage at negative triaxiality, European Journal of Mechanics A/Solids 31 (2012) 203–212.

[63] E. Smith, Cleavage fracture in mild steel, International Journal of Fracture Mechanics 4 (1968) 131–145.

[64] X. Gao, C. Shih, V. Tvergaard, A. Needleman, Constraint effects on the ductile-brittle transition in small scale yielding, Journal of Mechanics and Physics of Solids 44 (1996) 1255–1282.

[65] K. Shibanuama, S. Aihara, K. Suzuki, Prediction model on cleavage fracture initiation in steels having ferrite-cementite microstructures – Part I: Model presentation, Engineering Fracture Mechanics 151 (2016) 161–180.